J. Space Weather Space Clim. 2025, **15**, 10

https://doi.org/10.1051/swsc/2025008

JSWSC

Available online at:
www.swsc-journal.org

RESEARCH ARTICLE OPEN ACCESS

Estimation of the impact of solar flare spectra on the Earth's ionosphere using the GAIA model

Shinnosuke Kitajima[1,*], Kyoko Watanabe[1], Hidekatsu Jin[2], Chihiro Tao[2], and Michi Nishioka[2]

[1] National Defense Academy of Japan (NDA), Yokosuka 2398686, Japan
[2] National Institute of Information and Communications Technology (NICT), Koganei 1848795, Japan

Received 21 February 2024 / Accepted 26 February 2025

Abstract – The rapid increase in X-ray and extreme ultraviolet (EUV) emissions owing to solar flares enhances ionization in the ionosphere, increasing radio wave attenuation. Among these phenomena, the shortwave communication disturbance caused by the increased electron density in the ionospheric D region is known as the shortwave fadeout (SWF). We investigated the relationship between SWF's magnitude and solar flare emission, and evaluated the electron density variation in the ionospheric D region associated with flare. We defined the minimum frequency (*f*min) observed in Japan's ionograms as the SWF's magnitude. We analyzed ionosonde data for 38 SWF events observed during daytime in Japan between May 2010 and May 2014. To investigate the relationship between flares and SWF, we compared the observed X-ray and EUV emissions during flares with the d*f*min (background subtracted *f*min). X-ray (0.1–0.8 nm) and EUV (11–14 nm) emissions correlate with d*f*min. Then, using the GAIA model, a numerical model that treats the entire Earth's atmosphere, we investigated the effect of the X-ray and EUV solar flare emissions on the ionosphere, which affects the SWF. The results showed that the main ionization source in the ionospheric D region was X-ray emission, and shortwaves were attenuated by ∼90%. In contrast, in the ionospheric E and F regions, the primary ionization source was EUV emission, with only ∼10% shortwave attenuation. Finally, we estimated the *f*min values and blackout (total fadeout of the ionospheric echo observed in ionograms) and compared the simulated and observed *f*min values. The hit rate of blackouts was 35% when we only used the GAIA calculations. Therefore, we estimated *f*min using the electron density variation in the ionospheric D region corresponding to X-ray solar emission. As a result, the hit rate of the blackout was 68%, and the linear correlation coefficient between the simulated and observed *f*min values was 0.85. The estimated magnitude of the SWF was improved by incorporating the effects of X-ray emissions into the ionospheric D region of GAIA. We are the first to implement a method for evaluating the electron density in the ionospheric D region using the *f*min value.

Keywords: Shortwave fadeout (SWF) / Dellinger phenomenon / Solar flare / Ionosphere / X-ray emission / EUV emission / Space weather

1 Introduction

In the Earth's atmosphere, there is a region called the ionosphere in which some atoms and molecules are ionized. Variations in the level of solar activity may lead to various space weather phenomena as well as fluctuations in the ionosphere. One such phenomenon is a shortwave communication failure, known as shortwave fadeout (SWF) or the Dellinger phenomenon (Dellinger, 1937). Shortwave communication is essential for disaster response and air traffic control. Statistical studies on SWF have shown they are related to solar flares (e.g., DeMastus and Wood, 1960). The September 2017 event is a well-known example of a disruption to shortwave communication. Multiple X-class solar flares occurred in September 2017. During the same period, multiple hurricanes struck areas near the Caribbean Sea and the Florida Peninsula in the United States. The damage caused by these hurricanes was severe, and shortwave communication systems were locally used for emergency disaster response. However, these shortwave communication systems were affected by SWF, rendering communication impossible for several hours (Redmon et al., 2018). Thus, space weather events with significant impacts can coincide with ground-based disasters (Rutledge and Desbios, 2018). In such circumstances, the impact of the SWF can be minimized if the available radio frequencies can be estimated. A clear

*Corresponding author: ed23002@nda.ac.jp; gekou.lol.shine@gmail.com

understanding of the causes of SWF is required to minimize the impact of such space weather events.

During solar flares, X-ray (0.1–10 nm) and extreme ultraviolet (EUV, 10–120 nm) emissions increase rapidly (e.g., Kelly and Rense, 1972; Horan et al., 1983; Fletcher et al., 2011) and instantly enhance ionization in the ionosphere (e.g., Rishbeth and Garriot, 1969; Thome and Wagner, 1971; Qian et al., 2011; Sojka et al., 2013). In the ionosphere, the composition and density distribution of atoms and molecules vary with altitude. The degree of ionization varies with altitude, depending on the spectrum and flux changes of solar emissions. For example, X-ray emission ionizes the O_2 and N_2, which are the main neutral components in the ionospheric D region (e.g., Mitra, 1974; Schumer, 2009). Because SWF is generally caused by a sudden increase in electron density in the ionospheric D region, a rapid increase in X-ray emissions due to solar flares is considered the main cause of SWF. Although the Lyman-α line peaks at a relatively long wavelength (121.6 nm), its emission ionizes NO. This means that Lyman-α emission may penetrate the Earth's atmosphere down to the lower atmosphere and affect the ionization of the atmosphere at altitudes in the ionospheric D region in addition to X-rays (e.g., Nicolet and Aikin, 1960). Moreover, it is generally known that Lyman-α under quiet conditions and X-rays during solar flares are critical solar emission lines that produce the ionospheric D region (e.g., Mitra, 1974; Schumer, 2009). In contrast, Milligan et al. (2020) reported that Lyman-α during solar flare is responsible for the ionospheric response by comparing the time profile of X-ray and Lyman-α with magnetometer data. At other wavelengths, Lyman-β (102.7 nm) is a significant source of ionization in the E region and He II (30.4 nm) in the F region (e.g., Mitra, 1974; Machol et al., 2020). Several studies have discussed the relationship between SWF and X-ray (e.g., Deshpande et al., 1972; Sato, 1975; Tao et al., 2020; Buzás et al., 2023). Manju et al. (2012) discussed the relationship between the ionospheric E and F region's responses and EUV solar flare emissions in 26–34 nm, which are observations in bands. In our study, we discuss the relationship between SWF and the X-ray and EUV solar flare spectrum, which contributes to ionospheric ionization.

One method to detect the magnitude of the SWF is from the minimum frequency (*f*min) observed in the ionograms. Because *f*min values vary with solar activity and seasonal and day-to-day variations, SWF was evaluated using d*f*min, the difference between *f*min value and the background (defined as the median value of *f*min over a 27-day period, specifically calculated from 13 days before and 13 days after the target day, at the same local time) of *f*min value. When solar flares occur, statistical studies have reported that the d*f*min value increases and its variation depends on the flare class (the maximum X-ray flux of the flare) and the solar zenith angle (e.g., Sato, 1975; Tao et al., 2020). However, in some cases, *f*min was not proportional to the flare class. The *f*min value of X-class flares was smaller than that of M-class flares, and the duration of SWFs by M-class flares was longer than that by X-class flares (see Table 3 of Barta et al. (2019); Figs. 3, 6 of Tao et al. (2020)). Although the flare class alone is insufficient to estimate the *f*min, the impact of EUV emissions on *f*min has not yet been investigated. Therefore, we need to investigate the association between the time profile of X-ray and *f*min more closely. Investigating whether X-rays and other flare-origin emissions may impact *f*min values is also necessary.

This study has two main objectives. The first objective is to investigate the wavelengths that mainly affect the SWF by comparing *f*min with fluxes of flare emission spectra from satellite data, and the second one is to evaluate the electron density in the ionospheric D region using a numerical model and signal from the ionosonde. We also evaluated the accuracy of estimating the magnitude of the SWF using a numerical model by estimating not only the *f*min but also the blackout (total fadeout of the ionospheric echo observed in ionograms) and comparing them with observations. No studies have evaluated numerical models by estimating *f*min and blackout using ionospheric parameters obtained from numerical simulations. The paper is organized as follows: In Section 2, we introduce the instruments and data used in this study; in Section 3, we describe the method to estimate the attenuation of the high-frequency (HF) and a numerical model used in this study; in Section 4, we show the result of comparing *f*min values with the fluxes of flare emissions; in Section 5, we simulate the ionospheric response and estimate the radio propagation using a numerical model; in Section 6, we estimate *f*min as the magnitude of SWF, and evaluate the electron density during the solar flare in the ionospheric D region.

2 Observational data and event selection

2.1 *f*min

The National Institute of Information and Communications Technology (NICT) operates ionosondes in Wakkanai (45.16°N, 141.75°E), Kokubunji (35.71°N, 139.49°E), Yamagawa (31.20°N, 130.62°E), and Okinawa (26.68°N, 128.15°E). An ionosonde produces a vertical ionospheric sound with a 1–30 MHz pulse signal. Examples of the observed ionogram data are in Figure 1. Figure 1 shows the sequence of ionograms in Kokubunji and Okinawa when the SWF occurred on May 13, 2013, with an X1.7 class flare. The upper figures show the ionograms before the flare began (1:45 UT), the middle figures show the ionograms at the flare peak (2:15 UT), and the lower figures show the ionograms at the end of the SWF (3:45 UT). The *f*min values of Wakkanai, Yamagawa, and Okinawa in this event are 1.71 MHz, 3.14 MHz, and 4.30 MHz at 1:45 UT, no values of *f*min at 2:15 UT, and 3.51 MHz, 4.35 MHz, and 5.15 MHz at 3:45 UT, respectively. The total fadeout of the ionospheric echo observed in the ionograms at 2:15 UT is called a blackout. The ionograms of Kokubunji have intense background noise in the range of 1–4 MHz, as shown in Figure 1. These ionograms are available on the NICT website and recorded every 15 min at each observatory. This study used *f*min values obtained from Wakkanai, Kokubunji, Yamagawa, and Okinawa ionograms. In the Kokubunji ionogram, we excluded the uncertain value of *f*min owing to overlap with noise.

*f*min values vary with solar activity and seasonal and day-to-day variations, as shown in Figure 2 of Tao et al. (2020): during the period 1981–2016. *f*min values were high from April to September in the Northern Hemisphere and during the daytime at 11:00–12:00 LT. These variations in *f*min values were the

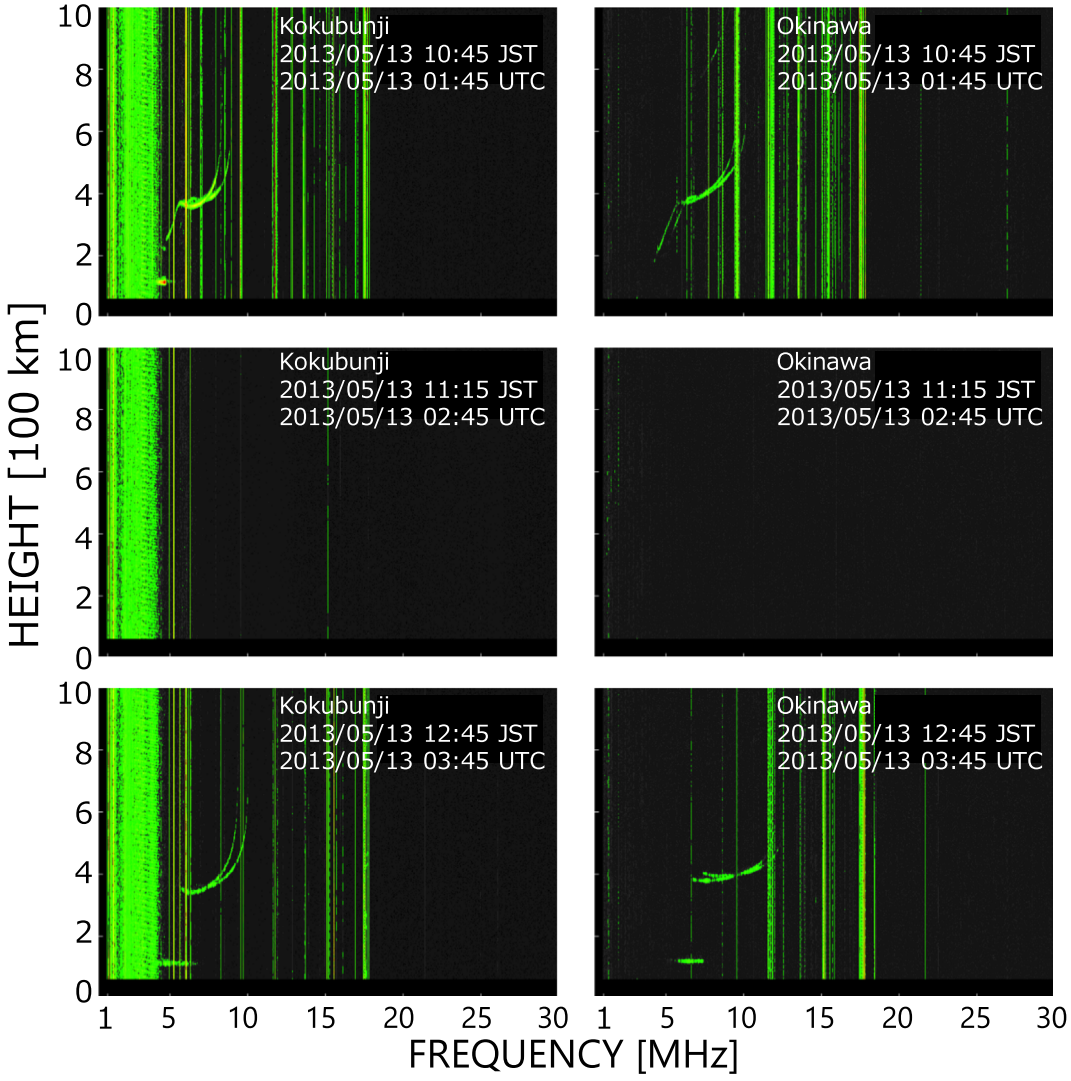

Figure 1. The sequence of ionograms during a solar flare occurred on May 13, 2013. The ionograms of Kokubunji and Okinawa are shown on the left and right of the pictures, respectively. The upper panels are the results before the flare began (1:45 UT), the middle panels are the results at the flare peak (2:15 UT), and the lower panels are the results at the end of the SWF (3:45 UT). The green curve and horizontal line represent the signal reflected in the ionosphere, and the vertical line is noise.

largest in the solar maxima. Therefore, we used d*f*min to quantify the effects of the solar flares. The d*f*min values of Wakkanai, Yamagawa, and Okinawa in the same event with Figure 1 are 0.21 MHz, 1.04 MHz, and 0.90 MHz at 1:45 UT, and 1.71 MHz, 1.65 MHz, and 0.95 MHz at 3:45 UT, respectively. Although the *f*min values vary with the ionosonde locations and are difficult to compare, d*f*min allows for comparison with ionosondes at different locations.

2.2 Solar flare flux data from satellites

In this study, we used X-ray and Lyman-α flux data obtained from the Geostationary Operational Environmental Satellite (GOES)/X-ray Sensor (XRS) and Extreme Ultraviolet Sensors with E-channel (EUVS-E), respectively. The flux of the EUV spectrum was obtained from the Solar Dynamics Observatory (SDO)/EUV Variability Experiment (EVE). These satellites have a geosynchronous orbit at an altitude of 35,789 km (22,238 miles). The impact on the Earth's ionosphere of the flux of solar flare emission that reaches the Earth's ionosphere depends on the solar zenith angle χ [rad]. Sato (1975) proposed that empirical relationships between the *f*min values and the solar flare flux are proportional to $\cos^{0.5}\chi$. Therefore, the solar zenith angle-corrected flare flux Fχ (solar flare flux multiplied by $\cos^{0.5}\chi$; Sato (1975)) was used in this study.

The GOES satellite is a geostationary orbiting satellite operated by the National Oceanic and Atmospheric Administration (NOAA) since 1975. The XRS observes X-ray fluxes in two wavelength bands from the entire solar surface at 0.05–0.4 nm and 0.1–0.8 nm (Bornmann et al., 1996). The 0.1–0.8 nm solar X-ray flux is used to classify the solar flare scale. The temporal resolution of the GOES X-ray data is 2 s.

The EUVS was installed at the GOES in 2006 to measure the flux of EUV emissions (Eparvier et al., 2009). The EUVS has five observation channels, A to E, covering wavelength ranges of 5–15 nm, 25–34 nm, 17–67 nm, 17–84 nm, and

118–127 nm, respectively. Among these channels, EUVS-E primarily observes Lyman-α radiation. The temporal resolution of GOES/EUVS-E data was 10 s.

The SDO satellite launched in February 2010 is a solar observation satellite (Woods et al., 2012). The EVE is an instrument that can measure the solar EUV emission spectrum, and the Multiple EUV Grating Spectrograph (MEGS) onboard the EVE observes solar EUV emission spectra in the 0.1–106 nm range. We used the MEGS-A and MEGS-B instruments, which observe solar EUV emission spectra in the 6–37 and 35–105 nm range, respectively. As MEGS-A is no longer in operation, we used in this study Level 2 spectra from the period May 1, 2010, to May 26, 2014, when the instrument was in operation. We used data with spectral resolutions of 0.1 nm and a time resolution of 10 s.

2.3 Event

The events analyzed in this study (see Table 1) were M3-class or larger flares that occurred during the daytime at Japan Standard Time (9:00–18:00 JST) from May 2010 to May 2014, when the SDO/EVE MEGS-A was in operation. Based on these criteria, 42 flare events were selected (Watanabe et al., 2012). In the case of multiple solar flares in one day, we defined SWF as one event. There were 1014 data points from 38 SWF events. Blackouts occurred in 66 of the 1014 data points. The d*f*min values were compared with the closest in-time satellite data. An example of the observed data is shown in Figure 2. Figure 2 shows the time profiles of the X-rays, EUV flux, and the time variation of the d*f*min value for the same flare event shown in Figure 1. As the flux increases, the d*f*min values either increase or disappear. A blackout occurred during the disappearance of the d*f*min values around 2:15 UT (Fig. 2e). The time profile of the flux during the solar flare varies with wavelengths of solar emissions. The time of peak flux for X-rays is 2:17 UT (Fig. 2a), and for EUV (11–14 nm) is 2:19 UT (Fig. 2c). In EUV (26–34 nm) and Lyman-α wavelengths, there is no apparent peak flux for this event (Fig. 2b and d). It is unclear which wavelengths have an impact on the d*f*min values.

3 Methods

3.1 Radio wave propagation in the ionosphere

When radio waves propagate through the ionosphere, various effects, such as fluctuations in electric and magnetic fields and energy loss due to collisions between electrons and neutral particles interact in complex ways. The Appleton-Hartree equations can describe the effect of these phenomena on radio propagation in cold plasma:

$$n^2 = 1 - \frac{X}{1 - iZ - \frac{Y_T^2}{2(1-X-iZ)} \pm \sqrt{\frac{Y_T^4}{4(1-X-iZ)^2} + Y_L^2}}, \quad (1)$$

where n is the refractive index, X is the plasma term, Y_T and Y_L are the magnetic field terms transverse (perpendicular) and longitudinal (parallel) to the radio, respectively, and Z is the collision term between the electron and neutral particles. These terms are expressed as $X = n_e e^2/m_e\varepsilon_0\omega^2$, $Y_T = \Omega_e sin\theta/\omega$, $Y_L = \Omega_e cos\theta/\omega$, $Z = \nu/\omega$, respectively, where n_e is the electron density, e is the electron's elementary charge, m_e is the electron mass, and ε_0 is the dielectric constant in vacuum, ω is the radio frequency, θ is the angle between the ambient magnetic field and the radio wave, Ω_e is gyrofrequency, ν is the collision frequency. From equation (1), two wave modes (the left-handed ordinary mode: L-O mode and the right-handed extraordinary mode: R-X mode) propagate in the ionosphere, which is a magnetized plasma. However, because *f*min could not clearly distinguish between the two wave modes, the data were provided as a mixture of the two wave modes. Assuming that the influence of the magnetic field is ignored ($\Omega_e = 0$), the approximation for non-magnetized plasma gives the attenuation between the two wave modes (Chum et al., 2018). We consider a non-magnetized plasma, and equation (1) can be rewritten as follows:

$$n^2 = 1 - \frac{n_e e^2/m_e\varepsilon_0\omega^2}{1 - i(\nu/\omega)}. \quad (2)$$

The radio waves were reflected at altitudes of $n = 0$. If the radio wave is a plane wave propagating in a particular direction (x), and the real ($\hat{n}$) and imaginary ($i\kappa$) values of the refractive index are expressed separately, then the equation of the radio wave for the electric field strength is as follows:

$$E = E_0 \exp(-\frac{\omega}{c}\kappa x) \exp i(\omega t - \frac{\omega\hat{n}}{c}x), \quad (3)$$

where c is light speed. The term $\exp(-\omega\kappa x/c)$ is the attenuation term for radio waves. By adding this attenuation term and the free-space propagation loss (Friis, 1946), we can estimate the attenuation in decibels of shortwave radio waves in the path of propagation through the ionosphere.

3.2 Numerical model: GAIA

Ionospheric parameters required to calculate the attenuation of radio waves may be obtained through numerical analysis. Physical models for calculating the upper atmosphere have been developed in many countries (e.g., Roble and Ridley, 1994; Akmaev et al., 2008; Liu et al., 2010). GAIA (Ground-to-Topside Model of Atmosphere and Ionosphere for Aeronomy; Jin et al., 2011; Miyoshi and Fujiwara, 2008) is a numerical model. GAIA was constructed to elucidate the coupling process between the upper and lower atmospheres, the interaction process between the neutral atmosphere and the ionosphere in the upper atmosphere, and the generation process of ionospheric and thermospheric disturbances associated with solar flares and magnetic storms. By combining an atmospheric model (Miyoshi and Fujiwara, 2003; Fujiwara and Miyoshi, 2006), an ionospheric model (Shinagawa and Oyama, 2006), and an electrodynamic model (Jin et al., 2008), GAIA is one of the models that can numerically simulate the entire region of Earth's atmosphere from the troposphere to the ionosphere. GAIA allows the input of solar emission spectra during solar flares and outputs the ionospheric response for each wavelength of the flare spectra. The flare EUV spectrum was obtained from FISM2 (The Flare Irradiance Spectral Model-Version 2; Chamberlin et al. (2020)). We input the flare EUV spectra into GAIA to

Table 1. List of selected events for this study.

Selected time period of ionogram [UT]	GOES [UT]			AR location	X-ray class
	Start	Peak	End		
2011 Feb 15 1:30–6:15	1:44	1:45	1:56	S20W10	X2.2
2011 Jul 30 2:00–3:45	2:04	2:09	2:12	N14E35	M9.3
2011 Aug 04 3:30–5:30	3:41	3:45	3:57	N16W38	M9.3
2011 Aug 09 7:45–9:00	7:48	8:05	8:08	N14W69	X6.9
2011 Sep 06 1:30–3:00	1:35	1:50	2:05	N13W07	M5.3
2011 Sep 25 2:15–6:00	2:27	2:33	2:37	N22W87	M4.4
	4:31	4:50	5:05	N13E50	M7.4
2011 Sep 26 5:00–6:45	5:06	5:08	5:13	N13E34	M4.0
2011 Oct 02 0:30–2:00	0:37	0:50	0:59	N10W14	M3.9
2011 Nov 05 3:00–5:00	3:08	3:31	3:58	N20E47	M3.7
2012 Jan 23 3:30–6:00	3:38	3:59	3:59	N33W21	M8.7
2012 Mar 05 2:30–6:45	2:30	4:05	4:43	N19E58	X1.1
2012 Mar 07 0:00–4:30	0:02	0:24	0:40	N18E31	X5.4
	1:05	1:14	1:23	N15E26	X1.3
2012 Mar 09 3:15–6:45	3:22	3:53	4:18	N15W03	M6.3
2012 May 10 4:00–5:45	4:11	4:18	4:23	N12E22	M5.7
2012 May 17 1:15–3:45	1:25	1:47	2:14	N07W88	M5.1
2012 Jul 05 3:15–4:30	3:25	3:36	3:39	S18W29	M4.7
2012 Jul 19 4:15–7:15	4:17	5:58	6:56	S13W88	M7.7
2012 Aug 18 0:15–1:30	0:24	1:02	1:07	N19E86	M5.5
2012 Oct 23 3:00–4:00	3:13	3:17	3:21	S13E58	X1.8
2012 Nov 13 1:45–4:00	1:58	2:04	2:06	S25E46	M6.0
2013 Apr 11 6:45–8:00	6:55	7:16	7:29	N09E12	M6.5
2013 May 10 0:30–1:30	0:44	0:57	1:08	N12E88	M3.9
2013 May 13 1:45–4:00	1:53	2:17	2:32	N11E89	X1.7
2013 May 14 0:00–3:45	0:00	1:11	1:20	N08E77	X3.2
2013 May 15 1:15–3:45	1:24	1:40	2:30	N12E64	X1.2
2013 May 17 8:30–9:00	8:43	8:57	9:19	N12E57	M3.2
2013 Oct 24 0:00–1:45	0:20	0:28	0:48	S10E08	M9.3
2013 Oct 25 7:45–8:45	7:53	8:01	8:09	S08E73	X1.7
2013 Oct 28 1:30–5:45	1:41	2:03	2:12	N04W66	X1.0
	4:32	4:39	4:53	N08W71	M5.1
2013 Nov 03 5:15–6:15	5:16	5:22	5:26	S12W16	M5.0
2013 Nov 08 4:15–5:15	4:20	4:26	4:29	S14E15	X1.1
2013 Nov 10 5:00–6:15	5:08	5:14	5:18	S14W13	X1.1
2014 Jan 08 3:30–4:15	3:39	3:47	3:54	N11W81	M3.6
2014 Feb 01 6:45–8:45	6:45	7:23	8:43	S11E23	M3.0
2014 Feb 04 1:15–4:45	1:16	1:23	1:31	S09W13	M3.8
	3:57	4:00	4:06	S14W06	M5.2
2014 Feb 12 3:45–5:45	3:52	4:25	4:38	S12W02	M3.7
2014 Feb 25 0:30–4:15	0:39	0:49	1:03	S12E82	X4.9
2014 Mar 11 3:30–6:00	3:44	3:50	4:29	N13W55	M3.5

calculate the altitude distribution of the ion production rate at different wavelengths of solar flare emissions and its temporal variation. Solomon and Qian (2005) provided the ionization cross-section used in GAIA. The ionospheric part of the GAIA has a vertical resolution of 10 km, horizontal resolution of 1° at latitude and 2.5° longitude, and a calculation altitude range of 0–3000 km. This model includes the photochemical reactions of respective ions (O^+, O_2^+, N^+, and N_2^+). The electron density (n_e) and collision frequency (ν) to be substituted into equation (2) were obtained from GAIA calculations. Figure 3 shows the results of the GAIA simulations for the same flare event, as in Figures 1 and 2. The left figure shows the difference in the ion production rates between 1:45 UT and 2:15 UT. The right figure shows the electron density in Okinawa at the same time as in Figures 1 and 2. 2:15 UT had the highest electron density in the ionospheric D region. The electron density at 3:45 UT was larger than that at 1:45 UT, which shows the same result as the sequence of ionograms in Figure 1.

4 Relationship between solar flare emissions and d*f*min

4.1 Relationship between X-ray flux and d*f*min

We used simple linear regression to evaluate the relationship between the fluxes of solar flare emissions and the d*f*min values. The results in this section have a very high statistical significance (p-value $\ll 0.001$). The flare class is known to correlate with the magnitude of the SWF and has been used to estimate it.

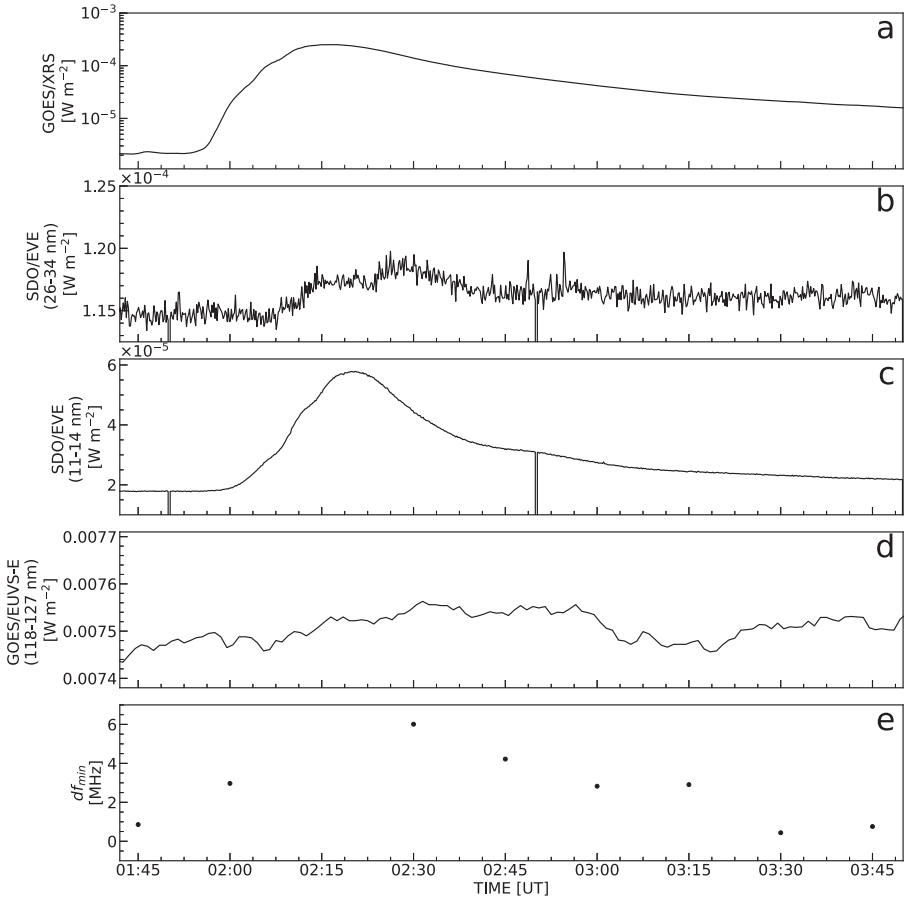

Figure 2. Time profiles for X-ray, EUV flux, and time variations of d*f*min on May 13, 2013. Panel a shows X-ray flux in 0.1–0.8 nm observed using GOES/XRS; panels b and c show EUV flux in 26–34 nm and 11–14 nm, respectively, observed using SDO/EVE; panel d shows Lyman-α flux observed using GOES/EUVS-E; panel e shows d*f*min values. The lack of d*f*min values in Okinawa at 2:15 UT indicates that the blackout occurred during this time.

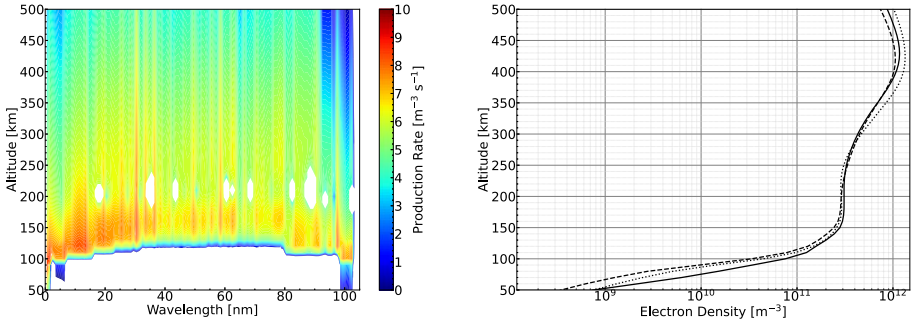

Figure 3. The results of GAIA simulations on May 13, 2013. The left figure shows the difference in the ion production rates between before the flare began (1:45 UT) and at the flare peak (2:15 UT). The right figure shows the electron density distributions. The dashed line is the electron density at 1:45 UT, the solid line is that at 2:15 UT, and the dotted line is that at the end of the SWF (3:45 UT).

In this study, we compared the zenith angle corrected X-ray (0.1–0.8 nm) flux with the d*f*min value simultaneously (Fig. 4). The linear correlation coefficient between d*f*min and X-ray flux was 0.77, indicating a good correlation. Tao et al. (2020) showed that, as a function of flare class, the standard deviation of d*f*min values increased for larger flares. By comparing the d*f*min values with the flux at time d*f*min, we found that the standard deviation hardly increased even when the solar flare flux was large compared to Tao et al. (2020).

4.2 Relationship between Lyman-α and d*f*min

Next, we compared d*f*min with the Lyman-α flux obtained using GOES/EUVS-E (Fig. 5). The linear correlation coefficient

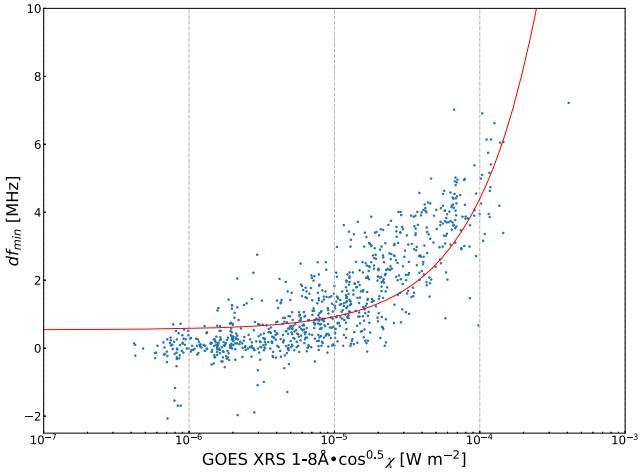

Figure 4. Relationship between the zenith angle corrected X-ray flux and d*f*min values. The solid red line is a best-fit line. The linear correlation coefficient between the X-ray flux and d*f*min value is 0.77.

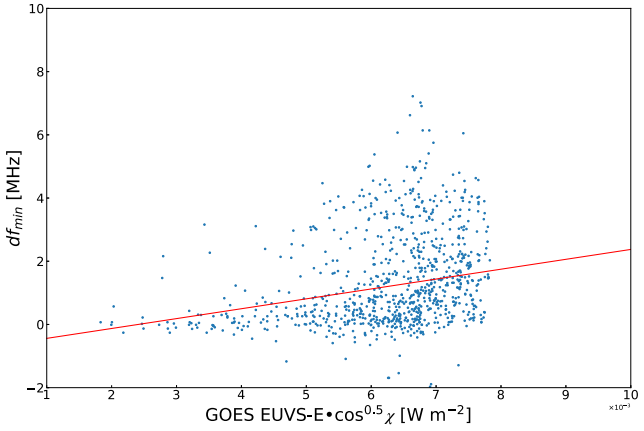

Figure 5. Relationship between the zenith angle corrected Lyman-α and d*f*min value. The solid red line is a best-fit line. The linear correlation coefficient between Lyman-α and d*f*min is 0.28.

between the zenith angle corrected Lyman-α and the d*f*min value was 0.28. Milligan et al. (2020) showed that the Lyman-α flare emission is significant for ionospheric disturbances, but we found no relationship between the Lyman-α flare emission and the d*f*min value in our study. The X-ray flux fluctuates by two to three orders of magnitude with the flare, whereas Lyman-α fluctuates by only about 10% or less. In addition, the Lyman-α variation was not synchronized with the X-ray variation and was inconsistent with the d*f*min variation. By comparing Figure 2a and d, the time of peak flux and the time profiles of the Lyman-α and the X-ray are significantly different. The X-ray flux and d*f*min values increased from 2:00 UT to 2:15 UT and decreased after 2:15 UT. On the other hand, the Lyman-α flux hardly varies at all. Moreover, X-rays ionize the O_2 and N_2, whose concentration is over 4 orders of magnitude higher than the NO (e.g., Mitra, 1974; Schumer, 2009). X-ray ionization in the ionospheric D region exceeds Lyman-α ionization during solar flares. Therefore, the lack of correlation between Lyman-α variations and d*f*min suggests that Lyman-α variations are small or almost constant during the flare and do not instantly enhance the electron density in the ionosphere. The results of Milligan et al. (2020) may result from the fact that the ionospheric response was caused by other EUV emissions similar to the time profile of Lyman-α emission.

4.3 Relationship between EUV and d*f*min

To investigate their linear correlation coefficients, we compared the flare EUV emission spectra (6–106 nm) observed by the SDO/EVE with the d*f*min values. First, we compared the d*f*min values with the mean flux of the EUV emission spectra wavelength at 1 nm wide intervals from 6 to 106 nm (Fig. 6). The linear correlation coefficients were less than 0.6, except for the emissions at 9–14 nm. The linear correlation coefficients for the 11–12, 12–13, and 13–14 nm were 0.76, 0.80, and 0.81, respectively. In general, EUV emission is known to affect ionization at higher altitudes than in the ionospheric D region (e.g., Watanabe and Hinteregger, 1962; Mitra, 1974), suggesting that the 11–14 nm EUV emission, which contributes to the ionization of the ionospheric E region may also cause SWF.

Next, the EUV emission in the 11–14 nm range is further subdivided into EUV emission spectra for each 0.1 nm, and the correlation between each wavelength and d*f*min is investigated in detail. The results are presented in Figure 7. The circles in Figure 7 coincide with the EUV lines for Fe XIX-XXIII of the flare emission, which increased rapidly with the solar flares. Fe XIX-XXIII indicates iron between nineteen-times-ionized and twenty-three-times-ionized, emitted in the solar corona. X-rays are also emitted in the solar corona, and the time profiles of X-ray and Fe XIX-XXIII are almost similar. Therefore, both emissions are considered highly correlated with the d*f*min values.

5 Ionospheric response during flares by GAIA

We found two flare emissions, X-ray (0.1–0.8 nm) and EUV (11–14 nm), which would be the main factors for the occurrence of the SWF. We then ran simulations to advance our understanding of these observations and reveal the extent to which emissions contribute to the SWF in the ionosphere. Therefore, we simulated the ionospheric response to solar flare emissions using GAIA and compared the calculated results with observed data.

5.1 Ion production rate in the ionosphere during solar flare

Figure 8 shows the time profile of averaged ion production rates in the D (<100 km), E (100–150 km), and F (>150 km) regions of the ionosphere for X-ray (0.1–0.8 nm) and EUV (11–14 nm) emission for the same flare event as in Figure 3. In the D region, the averaged ion production rate by X-rays was approximately six orders of magnitude higher than that of the EUV emission. In E and F regions, the averaged ion

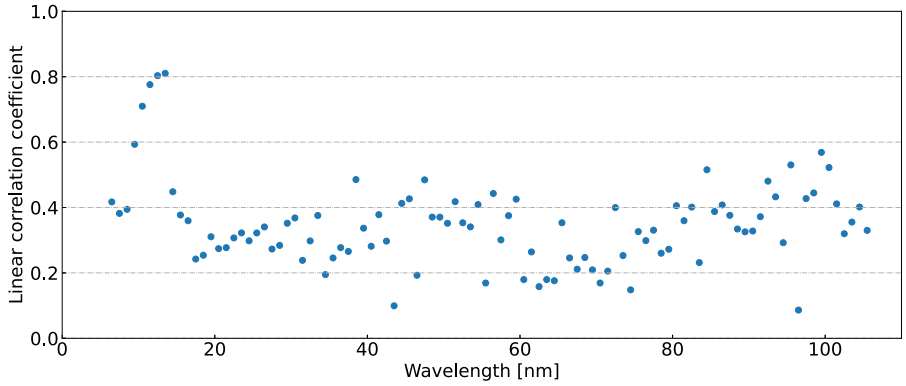

Figure 6. Linear correlation coefficient between the d*f*min and EUV emission spectra for every 1 nm.

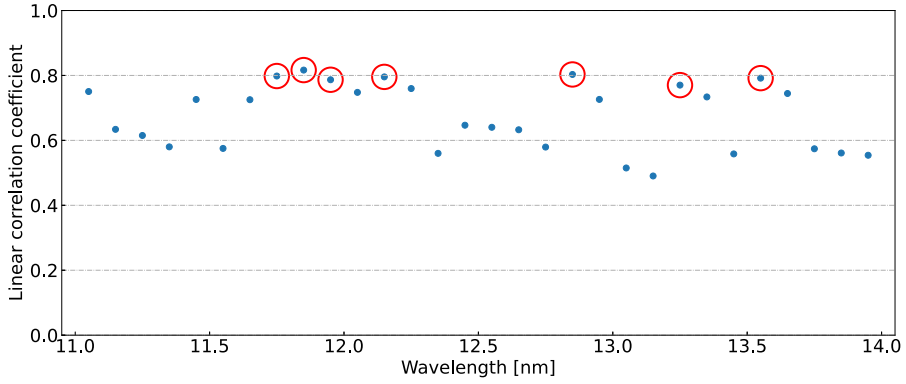

Figure 7. Linear correlation coefficient between d*f*min and EUV emission spectra every 0.1 nm. The red circles correspond to the EUV emission lines for Fe XIX-XXIII.

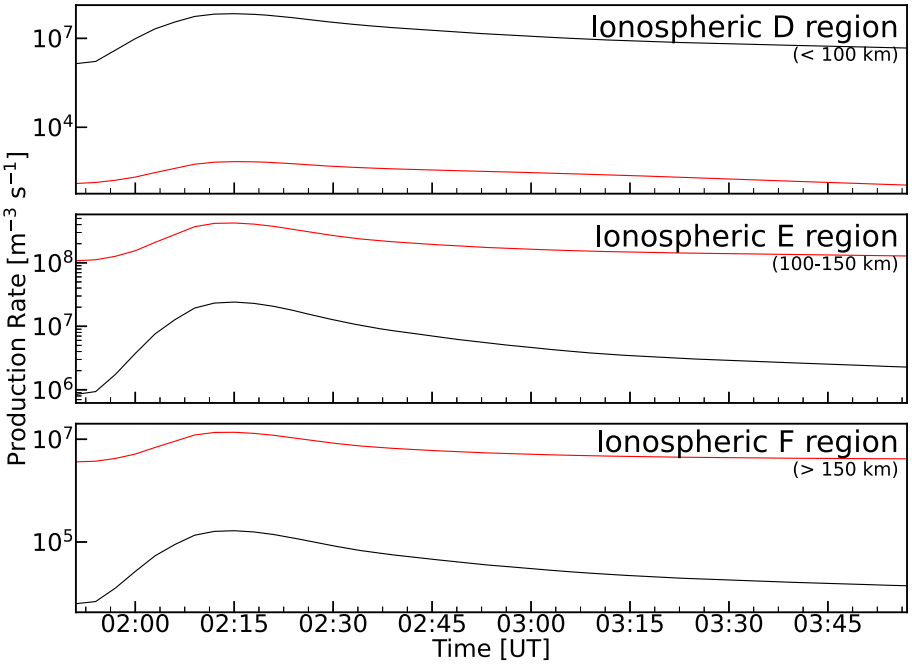

Figure 8. Temporal variation in averaged ion production rates in various ionospheric regions, as calculated using GAIA. The black solid line shows the averaged ion production rate from X-ray emission (0.1–0.8 nm) and the red solid line from EUV emission (11–14 nm).

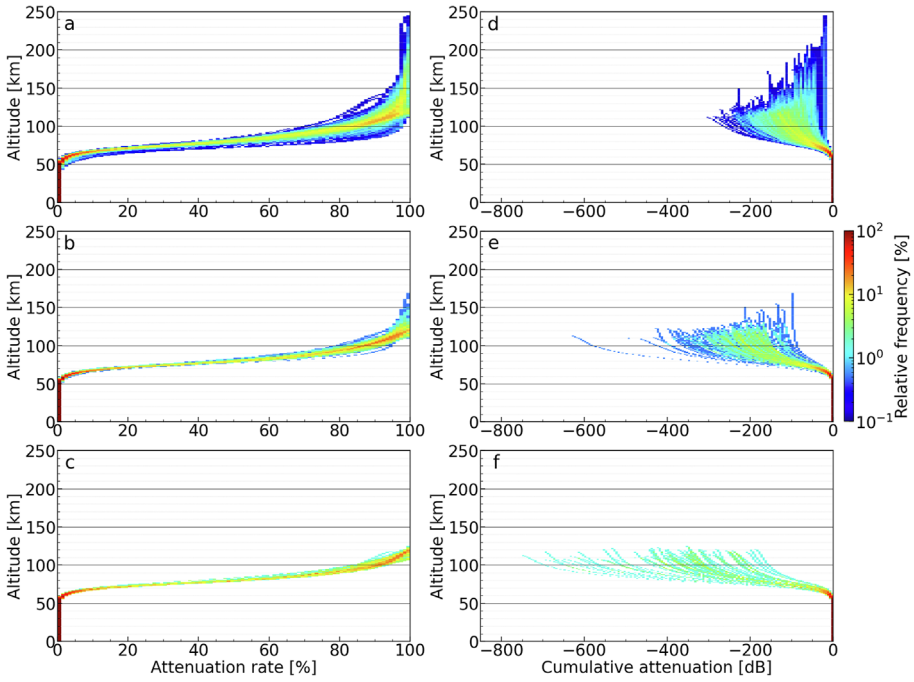

Figure 9. Altitude distribution of the attenuation rate and cumulative attenuation for 3 MHz in the ionosphere for all events. The left (a, b, c) and right panels (d, e, f) show the HF radio wave's attenuation rate and cumulative attenuation, respectively. Upper panels (a, d) are the results when d*f*min are less than 2.5 MHz, middle panels (b, e) are the results when d*f*min are 2.5 MHz or more, and lower panels (c, f) are the results at the blackouts.

production rate from EUV emission is about 1–2 orders of magnitude larger than that of X-rays. Therefore, these results show that the main source of ion density fluctuation is X-ray emission in the D region and EUV emission in the E and F regions (e.g., Rishbeth and Garriot, 1969; Thome and Wagner, 1971; Qian et al., 2011; Sojka et al., 2013).

5.2 Derivation of attenuation rate of HF radio waves

We considered radio wave propagation through the ionosphere using equations (2) and (3) to estimate the attenuation of the HF radio waves. The radio frequency (ω) corresponds to the pulse signal from ionosonde, and the electron density (n_e) and collision frequency (ν) are obtained from the GAIA results. The refractive index and attenuation of the radio waves can then be calculated using these values and equations. We estimated the attenuation of the HF radio waves. Specifically, 3 MHz, which is the lowest frequency in the frequency band of the HF radio wave region, was input for the values of ω, and the GAIA calculation results were input for the values of n_e and ν. We categorize the magnitude of SWFs with the criteria of d*f*min < 2.5 MHz, d*f*min $\geqq$ 2.5 MHz and blackout.

Figure 9 shows the altitude distributions of the attenuation rate and cumulative attenuation of HF radio waves considering upward and downward propagation in the ionosphere obtained from the simulations and calculations. As shown in Figure 9, the smaller the d*f*min values, the lower the cumulative attenuation (Fig. 9d and e), and the higher the altitude of the radio wave reflection (Fig. 9a and b). The attenuation of HF radio waves noticeably increases at altitudes >50 km and weakens above 100 km. ~90% of the 3 MHz signal attenuation occurred in the ionospheric D region (below 100 km altitude), and the remaining ~10% occurred in the ionospheric E and F regions (above 100 km altitude) during the blackout (Fig. 9c). However, for the HF radio signal at d*f*min < 2.5 MHz, the attenuation rate in the ionospheric D region decreases to ~80% (Fig. 9a). The cumulative attenuation during the blackout was approximately four times stronger than that at d*f*min < 2.5 (Fig. 9d and f). By contrast, when comparing the blackout and d*f*min ($\geqq$2.5 MHz), the cumulative attenuation was approximately 0.5 of that during the blackout (Fig. 9e and f).

The above results indicate that the contribution of X-ray emission to the SWF was approximately 90%. On the other hand, the HF radio waves in the ionospheric E and F regions are also attenuated by 10%. We suggest improving the accuracy of the estimation of the magnitude of the SWF, which is of primary importance for accurately simulating the electron density in the ionospheric D region using X-ray emissions from solar flares. Meanwhile, it is also necessary to consider the EUV emissions that affect the ionospheric E and F regions to improve the accuracy of estimating the SWF's magnitude.

6 Estimation of the magnitude of the SWF using GAIA

6.1 Evaluation of the estimated magnitude of the SWF

The SWF magnitude was estimated using GAIA calculations. First, the parameters of n_e and ν obtained from the GAIA calculations were input into equations (2) and (3), as described in Section 3, to derive the amount of radio wave attenuation.

The threshold for radio wave attenuation is the limit of attenuation in the radio propagation path between the transmitter and receiver. The value of the ionosonde allowed us to determine that the threshold for radio wave attenuation was −202 dB. We then determined the minimum value of ω that could be assumed to be reflected by the ionosphere and observed by the ionosonde, i.e., *f*min. The simulated *f*min can be considered as an estimation of the magnitude of the SWF. The estimated magnitude of the SWF was evaluated by comparing the simulated *f*min with the observed *f*min. The results of comparing the simulated *f*min with the observed *f*min are shown in Figure 10. As shown in Figure 10, the slope of the best-fit straight line is 1.09, the intercept is −0.64 MHz, and the linear correlation coefficient is 0.82. The simulated *f*min values estimated the observed *f*min values with high correlation. When we consider the occurrence of blackouts or non-blackouts, there are four classifications for blackout estimation: i) true positive (TP): blackouts are correctly estimated; ii) true negative (TN): non-blackouts are correctly estimated; iii) false positive (FP): blackouts are incorrectly estimated; and iv) false negative (FN): non-blackouts are incorrectly estimated. The number of TP, TN, FP, and FN was 23, 943, 43, and 5, respectively. The hit rate (ratio of TP to the total number of blackouts: TP/(TP + FP)) was 35%. These results indicate that the *f*min value can be used to estimate the magnitude of the SWF to some extent using GAIA calculations. However, the electron density during the flare in the ionospheric D region derived from the GAIA calculation was underestimated compared to the actual value.

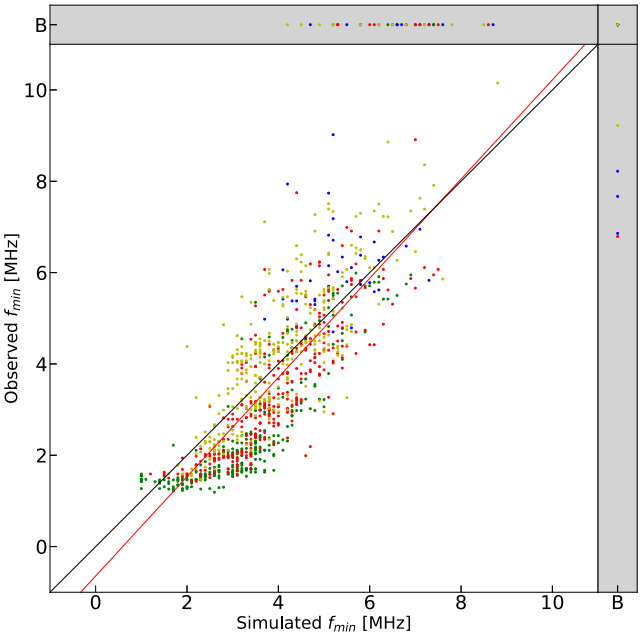

Figure 10. Comparison of simulated and observed *f*min values derived from GAIA. The solid red line is a best-fit straight line for the *f*min value, excluding blackout. The solid black line is a straight line with a slope of 1 and an intercept of 0. The gray shading indicates simulated and observed blackouts. Blackouts are shown as "B". The blue, green, red and yellow dots represent the *f*min values for Kokubunji, Wakkanai, Yamagawa, and Okinawa.

6.2 Electron density variations in the ionospheric D region during solar flare

To tackle the problem of the underestimation of electron density during solar flares, we created a function (*G(., Fχ)*) such that the electron density distribution in the ionospheric D region corresponded to the X-ray flux and altered it to the electron density in the GAIA simulation. The time variation of the solar zenith angle-corrected X-ray flux observed by GOES/XRS (Fχ) was used as a variable to determine the electron density. Therefore, we applied *G(., Fχ)* to the electron density distribution in the ionospheric D region (<100 km) during solar flares. A summary diagram of creating the *G(., Fχ)* is shown in Figure 11. First, we created the function *G(.)*, similar to the electron density distribution from the GAIA calculation results before the flare began (black solid line) by combining logarithmic (red), power (blue), and linear (green) functions to pass through two points (black dots): the origin and the electron density at an altitude of 100 km calculated by GAIA (Fig. 11a). Figure 11b shows the time profile of Fχ. We obtain a value of the X-ray flux in Fχ to determine a function *G(., Fχ)* in Figure 11c, which uses the variable Fχ (the value of X-ray flux at determined time points) to provide ionization altitude function for each time point. The cyan, magenta, and yellow functions of Figure 11c correspond to the points shown in Figure 11b. As shown in Figure 11b and c, *G(., Fχ)* was determined so that a larger Fχ affects the variation of electron density in the ionospheric D region. This reproduces the electron density variations in the ionosphere during the flare. The electron density in the ionospheric D region is the *G(., Fχ)* incorporating the variation by X-ray emission, and that in ionospheric E and F regions is simulated by GAIA. We evaluated the *G(., Fχ)* by comparing whether the simulated *f*min using the electron density of *G(., Fχ)* or GAIA-only more accurately estimates the observed *f*min.

The results of the comparison of the simulated *f*min using *G(., Fχ)* with the observed *f*min value are shown in Figure 12. As shown in Figure 12, the slope of the best-fit straight line between the simulated and observed *f*min values was 1.01, the intercept was −0.01 MHz, and the linear correlation coefficient was 0.85. The prediction accuracy of *f*min values exceeds that of the GAIA-only results. In particular, the number of TP, TN, FP, and FN were 45, 932, 21, and 16, respectively, the hit rate was 68%. The hit rate is better than the calculated GAIA value. We found that the estimated magnitude of the SWF was improved by incorporating the variation in the X-ray emission into the GAIA as information on the ionization in the ionospheric D region.

7 Conclusion

In this study, we investigated the relationship between solar flare emission spectra and SWF by comparing the fluxes of flare emissions from satellite data with *f*min. We also estimated the magnitude of the SWF from solar flare emissions using the GAIA model and evaluated the electron density. First, the X-ray flux correlated well with *f*min, with a linear correlation coefficient of 0.77. However, Lyman-α, known to contribute to the formation of the ionospheric D region, did not correlate

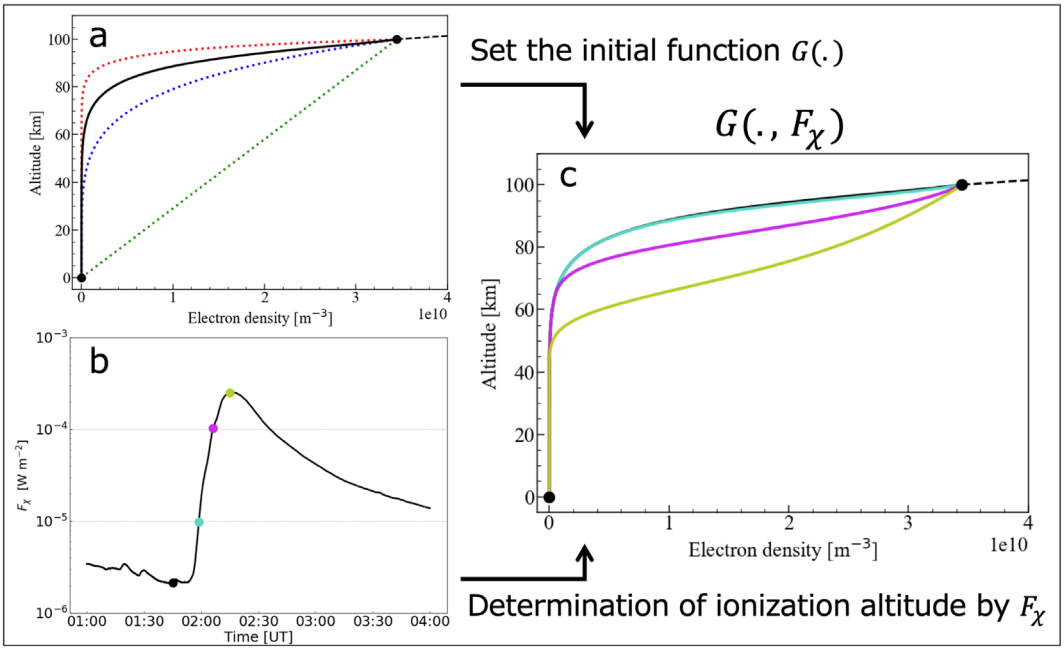

Figure 11. A summary diagram of electron density variations due to *G(., Fχ)*. Panel a shows the *G(.)* function representing electron density below 100 km altitude (black solid line) that is set by a combination of a logarithmic function (red dotted line), a power function (blue dotted line), and a linear function (green dotted line) passing through two points: the origin and the electron density value at 100 km altitude calculated using GAIA. Panel b shows the time variation of Fχ associated with the flare. Panel c is the electron density variation created by combining the function *G(.)* set in panel a and the ionization altitude corresponding to Fχ in panel b. The black dotted line is the electron density calculated using GAIA. The solid lines of cyan, magenta, and yellow in panel c are the functions *G(., Fχ)*, which correspond to the points shown in panel b.

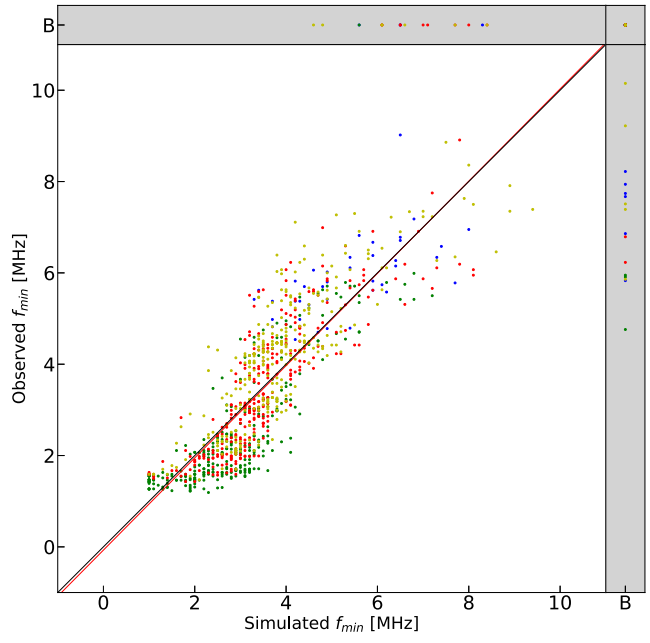

Figure 12. Comparison of simulated and observed *f*min values derived from GAIA and Fχ. The solid red line is a best-fit straight line for the *f*min value, excluding blackout. The solid black line is a straight line with slope 1 and intercept 0. The gray shading indicates simulated and observed blackouts. Blackouts are shown as "B". The blue, green, red and yellow dots represent the *f*min values for Kokubunji, Wakkanai, Yamagawa and Okinawa.

with *f*min (linear correlation coefficient of 0.28). This is consistent with the results that the D region response to solar flares, as measured by VLF amplitude observations, shows a good agreement with X-ray flare emissions but does not show a good correlation with Lyman-α (e.g., Raulin et al., 2013). Because the flux in Lyman-α shows small variations and ionizations during solar flares as compared X-ray flux, there is hardly any impact of the Lyman-α line on the variation of *f*min.

Next, focusing on EUV emission, EUV emission at wavelengths longer than 14 nm showed no correlation with *f*min, with a linear correlation coefficient of less than 0.6. However, the EUV emission band at 11–14 nm corresponding to the EUV emission lines of Fe XIX-Fe XXIII showed an excellent correlation with *f*min, with a linear correlation coefficient of 0.80. Therefore, we calculated the ion production rates for each flare emission wavelength and the attenuation rate of HF radio waves in each ionospheric region using GAIA. The main source of ion density fluctuation, which is the X-ray emission in the D region and the EUV emission in the E and F regions, is consistent with previous studies (e.g., Rishbeth and Garriot, 1969; Thome and Wagner, 1971; Mitra, 1974; Qian et al., 2011; Sojka et al., 2013).

The HF radio waves at 3 MHz were primarily attenuated in the ionospheric D region (50–100 km altitude), and their contribution to the SWF was approximately 90%, with the remaining about 10% originating from the ionospheric E and F regions during the blackout. The increase of the contribution to HF radio attenuation in the ionospheric D region is due to the increase of the electron density in the ionospheric D region,

which is consistent with the result of Figure 7 of Chum et al. (2018). Several studies describe the relationship between X-ray flare emission and SWF (e.g., Deshpande et al., 1972; Mitra, 1974; Sato, 1975; Tao et al., 2020; Buzás et al., 2023). In this study, by investigating the variations of d*f*min and HF radio attenuation with the flux of the solar flare spectrum, we clarify that X-rays are the main source of solar flare emissions that affect SWF. To further improve the accuracy of estimating the magnitude of the SWF, we should target the time profile of X-ray emissions, as in the present study, rather than the flare class as proposed in previous studies such as Barta et al. (2019) and Tao et al. (2020). Also, it is necessary to consider the EUV emissions of solar flares that affect the ionospheric E and F regions, which account for the remaining 10% of the attenuation.

Finally, we used the GAIA model to estimate the magnitude of the SWF and compared the simulated and observed *f*min values. In addition, we evaluated the electron density in the ionospheric D region. The correlation coefficient between the simulated and observed *f*min values was 0.82, and the hit rate was 35%. These results showed that the electron density values calculated by GAIA, especially in the ionospheric D region, were underestimated compared to the actual values. Therefore, we attempted to reproduce the electron density distribution during flares by using the time variation of the electron density in the ionospheric D region, which more directly considers the effect of X-ray emission. To reproduce the electron density distribution, we used a variable for the time variation of Fχ. As a result, the correlation coefficient between the simulated and observed *f*min values was 0.85, and the hit rate was 68%. These results indicate that the prediction accuracy of the *f*min value can be improved by incorporating the effect of X-ray emissions on the electron density fluctuations in the ionospheric D region during the flare. We found that it is possible to evaluate the electron density during solar flare, including the one from ionospheric D region, using *f*min and simulation from numerical models.

Acknowledgements

The authors would like to thank K. Nozaki for providing the information on ionozonde. This work was carried out by the joint research program of the Institute for Space–Earth Environmental Research (ISEE), Nagoya University. The SDO/EVE level 2 data version 7 data are available at http://lasp.colorado.edu/eve/data_access/eve_data/products/level2/. FISM data are available at https://lasp.colorado.edu/eve/data_access/evewebdata/fism/flare_hr_data/. The flare event data used in this study are available at https://hinode.isee.nagoya-u.ac.jp/flare_catalogue/. The ionogram data are available at https://wdc.nict.go.jp/Ionosphere/en/archive/. This study was supported by JSPS KAKENHI Grant Numbers JP22K03710. The authors declare that they have no competing interests. The editor thanks two anonymous reviewers for their assistance in evaluating this paper.

References

Akmaev RA, Fuller-Rowell TJ, Wu F, Forbes JM, Zhang X, Anghel AF. 2008. Tidal variability in the lower thermosphere: comparison of whole atmosphere model (WAM) simulations with observations from TIMED. *Geophys Res Lett* **35(3)**: L03810. http://dx.doi.org/10.1029/2007GL032584.

Barta V, Sátori G, Berényi KA, Kis Á, Williams E. 2019. Effects of solar flares on the ionosphere as shown by the dynamics of ionograms recorded in Europe and South Africa. *Ann Geophys* **37**: 747–761. http://dx.doi.org/10.5194/angeo-37-747-2019.

Bornmann PL, Speich D, Hirman J, Matheson L, Grubb R, et al. 1996. GOES x-ray sensor and its use in predicting solar-terrestrial disturbances. In: Washwell ER (Ed.), *GOES-8 and beyond*, vol. 2812. International Society for Optics and Photonics, SPIE, pp. 291–298. http://dx.doi.org/10.1117/12.254076.

Buzás A, Kouba D, Mielich J, Burešová D, Mošna Z, et al. 2023. Investigating the effect of large solar flares on the ionosphere based on novel Digisonde data comparing three different methods. *Front Astron Space Sci* **10**: 1201625. http://dx.doi.org/10.3389/fspas.2023.1201625.

Chamberlin PC, Eparvier FG, Knoer V, Leise H, Pankratz A, et al. 2020. The flare irradiance spectral model-version 2 (FISM2). *Space Weather* **18(12)**: e2020SW002588. http://dx.doi.org/10.1029/2020SW002588.

Chum J, Urbář J, Laštovička J, Cabrera MA, Liu J-Y, et al. 2018. Continuous Doppler sounding of the ionosphere during solar flares. *Earth Planets Space* **70(198)**: 1–19. http://dx.doi.org/10.1186/s40623-018-0976-4.

Dellinger JH. 1937. Sudden ionospheric disturbances. *Terr Magn Atmos Electr* **42(1)**: 49–53. http://dx.doi.org/10.1029/TE042i001p00049.

DeMastus H, Wood M. 1960. Short-wave fadeouts without reported flares. *J Geophys Res (1896–1977)* **65(2)**: 609–611. http://dx.doi.org/10.1029/JZ065i002p00609.

Deshpande SD, Subrahmanyam CV, Mitra AP. 1972. Ionospheric effects of solar flares-I. The statistical relationship between X-ray flares and SID's. *J Atmos Terr Phys* **34(2)**: 211–227. http://dx.doi.org/10.1016/0021-9169(72)90165-1.

Eparvier FG, Crotser D, Jones AR, McClintock WE, Snow M, Woods TN. 2009. The extreme ultraviolet sensor (EUVS) for GOES-R. In: Fineschi S, Fennelly JA (Eds.), *Solar physics and space weather instrumentation III*, vol. 7438. International Society for Optics and Photonics, SPIE, p. 743804. http://dx.doi.org/10.1117/12.826445.

Fletcher L, Dennis BR, Hudson HS, Krucker S, Phillips K, et al. 2011. An observational overview of solar flares. *Space Sci Rev* **159**: 19–106. http://dx.doi.org/10.1007/s11214-010-9701-8.

Friis HT. 1946. A note on a simple transmission formula. *Proc IRE* **34(5)**: 254–256. http://dx.doi.org/10.1109/JRPROC.1946.234568.

Fujiwara H, Miyoshi Y. 2006. Characteristics of the large-scale traveling atmospheric disturbances during geomagnetically quiet and disturbed periods simulated by a whole atmosphere general circulation model. *Geophys Res Lett* **33(20)**: L20108. http://dx.doi.org/10.1029/2006GL027103.

Horan DM, Kreplin RW, Dere P. 1983. Direct measurements of the gradual extreme ultraviolet emission from large solar flares. *Sol Phys* **85(2)**: 303–312. http://dx.doi.org/10.1007/BF00148656.

Jin H, Miyoshi Y, Fujiwara H, Shinagawa H. 2008. Electrodynamics of the formation of ionospheric wave number 4 longitudinal structure. *J Geophys Res Space Phys* **113(A9)**: A09307. http://dx.doi.org/10.1029/2008JA013301.

Jin H, Miyoshi Y, Fujiwara H, Shinagawa H, Terada K, et al. 2011. Vertical connection from the tropospheric activities to the ionospheric longitudinal structure simulated by a new Earth's whole atmosphere-ionosphere coupled model. *J Geophys Res Space Phys* **116(A1)**: A01316. http://dx.doi.org/10.1029/2010JA015925.

Kelly PT, Rense WA. 1972. Solar flares in the EUV observed from OSO-5. *Sol Phys* **26**: 431–440. http://dx.doi.org/10.1007/BF00165285.

Liu HL, Foster BT, Hagan ME, Mclnerney JM, Maute A, et al. 2010. Thermosphere extension of the whole atmosphere community climate model. *J Geophys Res Space Phys* **115(A12)**: A12302. http://dx.doi.org/10.1029/2010JA015586.

Machol JL, Eparvier FG, Viereck RA, Woodraska DL, Snow M, et al. 2020. Chapter 19 – GOES-R series solar X-ray and ultraviolet irradiance. In: *The GOES-R series*. Elsevier, Amsterdam, Netherlands, pp. 233–242. http://dx.doi.org/10.1016/B978-0-12-814327-8.00019-6.

Manju G, Simi KG, Prabhakaran Nayar S. 2012. Analysis of solar EUV and X-ray flux enhancements during intense solar flare events and the concomitant response of equatorial and low latitude upper atmosphere. *J Atmos Sol Terr Phys* **86**: 1–5. http://dx.doi.org/10.1016/j.jastp.2012.05.008.

Milligan R, Hudson HS, Chamberlin PC, Hannah IG, Hayes LA. 2020. Lyman-alpha variability during solar flares over solar cycle 24 using GOES-15/EUVS-E. *Space Weather* **18(7)**: e2019SW002331. http://dx.doi.org/10.1029/2019SW002331.

Mitra AP. 1974. *Ionospheric effects of solar flares*. Springer Dordrecht. http://dx.doi.org/10.1007/978-94-010-2231-6.

Miyoshi Y, Fujiwara H. 2003. Day-to-day variations of migrating diurnal tide simulated by a GCM from the ground surface to the exobase. *Geophys Res Lett* **30(15)**: 1789. http://dx.doi.org/10.1029/2003GL017695.

Miyoshi Y, Fujiwara H. 2008. Gravity waves in the thermosphere simulated by a general circulation model. *J Geophys Res Atmos* **113(D1)**: D01101. http://dx.doi.org/10.1029/2007JD008874.

Nicolet M, Aikin AC. 1960. The formation of the D region of the ionosphere. *J Geophys Res (1896–1977)* **65(5)**: 1469–1483. http://dx.doi.org/10.1029/JZ065i005p01469.

Qian L, Burns AG, Chamberlin PC, Solomon SC. 2011. Variability of thermosphere and ionosphere responses to solar flares. *J Geophys Res Space Phys* **116(A10)**: A10309. http://dx.doi.org/10.1029/2011JA016777.

Raulin JP, Trottet G, Macotela M, Macotela EL, Pacini A, et al. 2013. Response of the low ionosphere to X-ray and Lyman-α solar flare emissions. *J Geophys Res Space Phys* **118(1)**: 570–575. http://dx.doi.org/10.1029/2012JA017916.

Redmon RJ, Seaton D, Steenburgh R, He J, Rodriguez JV. 2018. September 2017's geoeffective space weather and impacts to caribbean radio communications during hurricane response. *Space Weather* **16(9)**: 1190–1201. http://dx.doi.org/10.1029/2018SW001897.

Rishbeth JA, Garriot OK. 1969. III. Photochemical processes in the ionosphere. In: *Introduction to ionospheric physics*, vol. 14 of International Geophysics. Academic Press, Cambridge, Massachusetts, United States, pp. 87–125. http://dx.doi.org/10.1016/S0074-6142(09)60023-1.

Roble R, Ridley E. 1994. A thermosphere-ionosphere-mesosphere-electrodynamics general circulation model (time-GCM): equinox solar cycle minimum simulations (30–500 km). *Geophys Res Lett* **21(6)**: 417–420. http://dx.doi.org/10.1029/93GL03391.

Rutledge R, Desbios S. 2018. *Space weather focus: impacts of a severe space weather event on aviation operations*. World Meteorological Organization Commission for Aeronautical Meteorology (CAeM) Newsletter. https://mailchi.mp/f7811e0713c9/wmo-caem-newsletter-issue-12018.

Sato T. 1975. Sudden *f*min enhancements and sudden cosmic noise absorptions associated with solar X-ray flares. *J Geomagn Geoelectr* **27(2)**: 95–112. http://dx.doi.org/10.5636/jgg.27.95.

Schumer EA. 2009. Improved modeling of midlatitude D region ionospheric absorption of high frequency radio signals during solar X-ray flares. Ph.D. thesis, Air Force Institute of Technology. 2155, pp. 6–8. https://scholar.afit.edu/etd/2155/.

Shinagawa H, Oyama S. 2006. A two-dimensional simulation of thermospheric vertical winds in the vicinity of an auroral arc. *Earth Planets Space* **58**: 1173–1181. http://dx.doi.org/10.1186/BF03352007.

Sojka JJ, Jensen J, David M, Schunk RW, Woods T, Eparvier F. 2013. Modeling the ionospheric E and F1 regions: using SDO-EVE observations as the solar irradiance driver. *J Geophys Res Space Phys* **118(8)**: 5379–5391. http://dx.doi.org/10.1002/jgra.50480.

Solomon SC, Qian L. 2005. Solar extreme-ultraviolet irradiance for general circulation models. *J Geophys Res Space Phys* **110(A10)**: A10306. . http://dx.doi.org/10.1029/2005JA011160.

Tao C, Nishioka M, Saito S, Shiota D, Watanabe K, et al. 2020. Statistical analysis of short-wave fadeout for extreme space weather event estimation. *Earth Planets Space* **72(173)**: 1–16. http://dx.doi.org/10.1186/s40623-020-01278-z.

Thome GD, Wagner LS. 1971. Electron density enhancements in the E and F regions of the ionosphere during solar flares. *J Geophys Res (1896–1977)* **76(28)**: 6883–6895. http://dx.doi.org/10.1029/JA076i028p06883.

Watanabe K, Hinteregger HE. 1962. Photoionization rates in the E and F regions. *J Geophys Res (1896–1977)* **67(3)**: 999–1006. http://dx.doi.org/10.1029/JZ067i003p00999.

Watanabe K, Masuda S, Segawa T. 2012. Hinode flare catalogue. *Sol Phys* **279**: 317–322. http://dx.doi.org/10.1007/s11207-012-9983-y.

Woods TN, Eparvier FG, Hock R, Jones AR, Woodraska D, et al. 2012. Extreme ultraviolet variability experiment (EVE) on the solar dynamics observatory (SDO): overview of science objectives, instrument design, data products, and model developments. *Sol Phys* **275**: 115–143. http://dx.doi.org/10.1007/s11207-009-9487-6.

Cite this article as: Kitajima S, Watanabe K, Jin H, Tao C & Nishioka M, et al. 2025. Estimation of the impact of solar flare spectra on the Earth's ionosphere using the GAIA model. *J. Space Weather Space Clim.* **15**, 10. https://doi.org/10.1051/swsc/2025008.